Nanoscale Advances

ROYAL SOCIETY OF CHEMISTRY

PAPER

View Article Online
View Journal | View Issue

Cite this: *Nanoscale Adv.*, 2022, **4**, 2196

Differential copper-guided architectures of amyloid β peptidomimetics modulate oxidation states and catalysis†

Debasis Ghosh, Mouli Konar, Tanmay Mondal and Thimmaiah Govindaraju *

Orchestration of differential architectures of designer peptidomimetics that modulate metal oxidation states to perform multiple chemical transformations remains a challenge. Cu-chelation and self-assembly properties of amyloid β (Aβ14-23) peptide were tuned by the incorporation of cyclic dipeptide (CDP) and pyrene (Py) as the assembly directing and reporting units, respectively. We explore the molecular architectonics of Aβ14-23 derived peptidomimetics ($Akd^{NMC}Py$) to form differential architectures that stabilize distinct Cu oxidation states. The fibrillar self-assembly of $Akd^{NMC}Py$ is modulated to form nanosheets by the one-off addition of Cu^{II}. Notably, the serial addition of Cu^{II} resulted in the formation of micelle-like core–shell architectures. The micelle-like and nanosheet architectures were found to differentially stabilize Cu^{II} and Cu^{I} states and catalyze tandem oxidative-hydrolysis and alkyne–azide cycloaddition reactions, respectively.

Received 15th March 2022
Accepted 30th March 2022

DOI: 10.1039/d2na00161f

rsc.li/nanoscale-advances

Introduction

The controlled organization of designer molecular building blocks to generate well-defined material architectures with unique functional properties and applications is the guiding principle of molecular architectonics.[1–3] Molecular recognition driven self-assembly and co-assembly through controlled non-covalent interactions are indispensable in the construction of diverse architectures. In the scheme of molecular architectonics, biomolecules play a key role as functional auxiliaries.[4] The self-assembly of peptides and proteins has been shown to produce structurally and functionally diverse multifunctional architectures with potential applications in the fields of opto-electronics, sensing, bioimaging and biomaterials.[5,6] Linear and cyclic peptides are attractive molecular building blocks to construct biomaterial scaffolds owing to their functional tolerability, ease of synthesis, biocompatibility, and enzyme mimetic ability.[7,8] The self-assembly of amyloid-forming short and oligopeptides and peptidomimetics produces catalytic amyloids in the presence of metal ions with catalytic activity in various hydrolytic and redox chemical transformations.[9–12] Ventura *et al.* recently demonstrated a pH dependent assembly of a short peptide with two divergent catalytic activities.[13] Recently, CDPs are being used as versatile building blocks and auxiliaries to construct functional architectures.[14,15] Gazit *et al.* reported a CDP-based nano-superstructure with efficient catalysis in the hydrolysis of *para*-nitrophenol acetate.[16] The potential of CDP-driven assembly architectures as catalytic systems in multiple chemical reactions is largely unexplored.

In the present work, we judiciously designed Aβ peptide-based CDP peptidomimetics and their metal-mediated assembly to produce differential architectures with distinct catalytic activities. We designed and synthesized peptidomimetics (Akd^{NMC} and $Akd^{NMC}Py$) of Aβ14-23 incorporated with unnatural CDP amino acid cyclo(L-Lys – L-Asp) (kd) and pyrene (Py) units at specific positions as shown in (Fig. 1 and S1†). Aβ14-23 (^{14}HQKLVFFAE^{23}D) has a self-recognition motif 'KLVFF' for amyloid assembly and metal-binding affinity.[17]

Metal chelation of Aβ14-23 through N-terminal histidine (^{14}H) prompted us to orchestrate its metal-directed assembly into differential functional architectures. To strengthen metal chelation and assembly, Aβ14-23 was incorporated with Py at the N-terminal and three kd units at the middle, and N and C-termini to obtain $Akd^{NMC}Py$ (Fig. 1).[18] The kd with a rigid ring-core and multiple hydrogen bonding and metal coordinating sites (amide linkages) was anticipated to influence metal binding and self-assembly of $Akd^{NMC}Py$. The fluorescent Py assists the monitoring of metal binding-mediated assembly of $Akd^{NMC}Py$ through its characteristic spectral properties. We investigated the molecular architectonics of $Akd^{NMC}Py$ upon binding to Cu^{II} in phosphate buffer saline (PBS, 10 mM, pH 7.4) (Fig. S2†). Cu is an important biocatalytic metal and capable of orchestrating distinct architectures with different oxidation states (Cu^{II} or Cu^{I}) and catalytic activity.[19]

We thus studied the assembly of $Akd^{NMC}Py$ (15 μM) by adding Cu^{II} in two distinct ways, (i) one-off addition: Cu^{II} (100

Bioorganic Chemistry Laboratory, New Chemistry Unit and School of Advanced Materials (SAMat), Jawaharlal Nehru Centre for Advanced Scientific Research, Jakkur P.O., Bengaluru 560064, Karnataka, India. E-mail: tgraju@jncasr.ac.in

† Electronic supplementary information (ESI) available. See DOI: 10.1039/d2na00161f

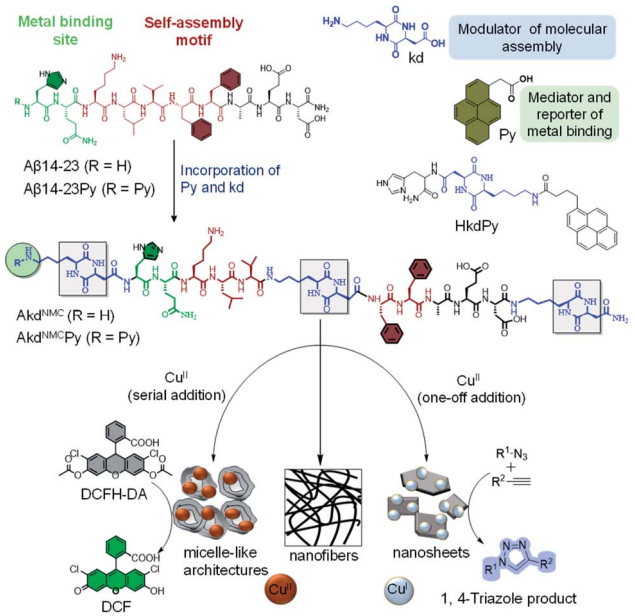

Fig. 1 Design of Aβ14-23 peptidomimetics (Akd^{NMC} and Akd^{NMC}Py) incorporated with kd and Py units. HkdPy is a model peptidomimetic. Molecular assembly of Akd^{NMC}Py in the absence and presence of one-off and serial additions of Cu^{II} to generate distinct architectures that stabilize Cu^{II} and Cu^{I} states with catalytic activity in tandem oxidative-hydrolysis of DCFDA and the alkyne–azide click reaction, respectively.

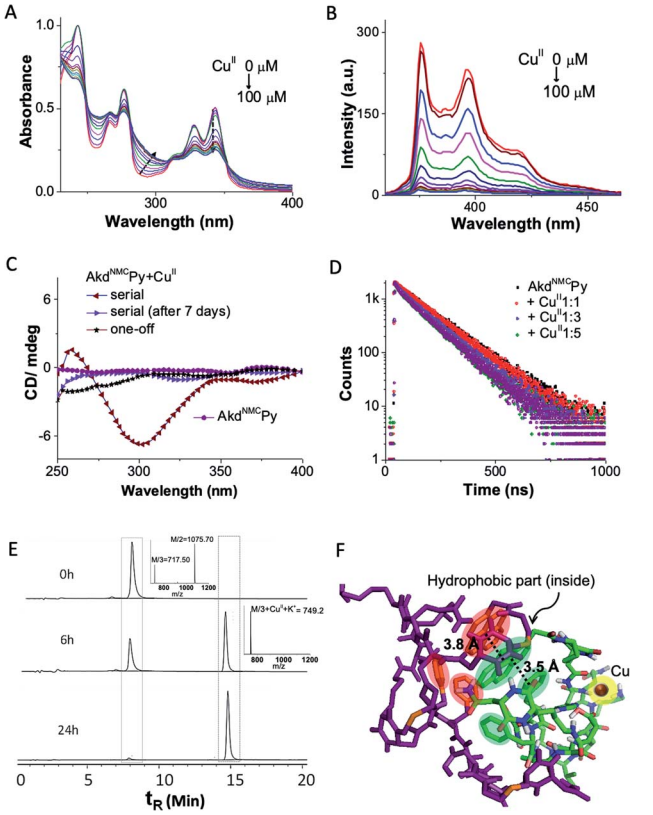

Fig. 2 (A) Absorbance, and (B) fluorescence spectra of Akd^{NMC}Py (15 μM) upon gradual addition of Cu^{II} (0 μM to 100 μM). (C) CD spectra of Akd^{NMC}Py and upon addition of Cu^{II} (one-off and serial additions). (D) Fluorescence lifetime measurements of Akd^{NMC}Py (λ_{ex} 343 nm) with Cu^{II}. (E) Time-dependent LC of Akd^{NMC}Py + Cu^{II} (inset MS data). (F) Molecular docking image of Akd^{NMC}Py + Cu^{II} and Akd^{NMC}Py with Py–Py and Py–Phe distances shown (dotted lines).

μM) was added in one shot, and (ii) serial addition: Cu^{II} (100 μM) was added as 20 aliquots of 5 μM each with an interval of 3.6 min (Fig. S3 and S4†). In the former case, Akd^{NMC}Py assembly progressed upon immediate complexation with Cu^{II} to produce stable 2D sheet architectures,[20,21] while the controlled complexation of Akd^{NMC}Py to Cu^{II} in the latter case resulted in stepwise assembly to form sheets *via* metastable micelle-like core–shell architectures. Interestingly, Cu^{II} was reduced to Cu^{I} during sheet formation, while micelle-like architectures retained the Cu^{II} state. The distinct architectures prompted us to exploit their functional utility in Cu^{II} and Cu^{I} catalysed tandem oxidative-hydrolysis, and alkyne–azide click reactions, respectively. To the best of our knowledge, this is the first report of metal-induced differential architectures of Aβ-peptidomimetics that stabilize Cu^{II} and Cu^{I} states to accomplish distinctive catalytic activities.

Results and discussion

We probed the complexation of Akd^{NMC}Py with Cu^{II} by UV-vis absorption, fluorescence, and circular dichroism (CD) in PBS (10 mM, 7.4 pH) (Fig. 2A–C). The Akd^{NMC}Py emission intensity in the 350–400 nm region (pyrene) was gradually quenched as a function of the Cu^{II} concentration with the corresponding enhancement in the absorption intensity around 280–290 nm. This is attributed to a change in the microenvironment of Phe (F) residues because of Cu^{II} complexation induced assembly of Akd^{NMC}Py. The absence of a Py excimer band ruled out possible Py–Py interactions. The decrease in the fluorescence lifetime (dynamic quenching) of Py (Akd^{NMC}Py) from 140.8 to 113.9 ns in the presence of Cu^{II} supported Py–Cu^{II} interaction (Fig. 2D and Table S1†).

This assumption was further supported by docking studies where Akd^{NMC}Py was blindly docked with Akd^{NMC}Py + Cu^{II}. The energy minimized docked pose showed a short F–Py distance (3.5 Å) as compared to the Py–Py distance (3.8 Å) (Fig. 2F, S5 and S6†).[22,23] We speculate that Akd^{NMC}Py adopted a spatial orientation to accommodate Cu^{II} that prevented Py–Py interaction while promoting F–Py interactions, as supported by the UV-vis absorption, fluorescence and docking studies.

The CD spectra revealed Cu^{II}-complexation-induced conformational change of Akd^{NMC}Py. A distinct negative CD band observed around 298 nm indicated the generation of a chiral environment due to Cu^{II} complexation-induced assembly of Akd^{NMC}Py. The spatial alignment of hydrophobic (F and Py) and hydrophilic moieties (–C=O of Asp, Glu and kd) of Akd^{NMC}Py in the energy minimized docked structure of Akd^{NMC}Py + Cu^{II} also suggested chirality induction upon complexation. Interestingly, the negative CD band at 298 nm disappeared over a period of 7 days suggesting two distinct assembly architectures for the Akd^{NMC}Py + Cu^{II} complex with initial chirally active and final chirally inactive states (Fig. 2C).[24] Fourier-transform infrared (FTIR) studies of Akd^{NMC}Py and the NMR spectrum of a model

peptidomimetic HkdPy with Cu^{II} confirmed the Cu^{II}–^{14}H ($Akd^{NMC}Py$) binding interactions (Fig. S7 and S8†).

The morphological outcomes of $Akd^{NMC}Py + Cu^{II}$ assemblies were investigated by time-dependent transmission electron microscopy (TEM) imaging over a period of 1 to 14 days. $Akd^{NMC}Py$ (15 μm) self-assembled to form fibrillar aggregates in PBS (Fig. S9†). One-off addition of Cu^{II} (100 μm) into $Akd^{NMC}Py$ (15 μm) resulted in the formation of stable nanosheets. Atomic force microscopy (AFM) has confirmed the formation of nanosheets with ~7 nm thickness and a 92.4 MPa DMT (Derjaguin–Muller–Toporov) modulus (Fig. 3A, S9 and S10†).[25] The powder X-ray diffraction (PXRD) and selected area electron diffraction (SAED) patterns suggested the crystalline nature of the nanosheets (Fig. 3A and S11†). Serial addition of Cu^{II} (20 aliquots of 5 μM each) to $Akd^{NMC}Py$ formed micelle-like core–shell architectures. The docking results have shown that the core pocket constitutes a hydrophobic region ($^{19}F^{20}F$ and Py), which is surrounded by the backbone and nucleophilic residues of $Akd^{NMC}Py$ to form Cu^{II}-induced micelle-like architectures. After 14 days of incubation, $Akd^{NMC}Py$ with serially added Cu^{II} (5 μM × 20 times) transformed from micelle-like architectures to 2D nanosheets (Fig. 3A). Field emission scanning electron microscopy (FESEM) images and the corresponding elemental mapping showed a higher Cu content in the micelle-like architecture compared to the nanosheets (Fig. S12†). We postulated that the micelle-like architectures formed initially were in a kinetically trapped metastable state, which restructured and transformed into thermodynamically stable 2D nanosheet architectures over time. Under similar conditions, $Akd^{NMC}Py + Cu^{I}$ (prepared by addition of $CuSO_4$ + sodium ascorbate to $Akd^{NMC}Py$), Aβ14-23, Aβ14-23Py, Akd^{NMC} and HkdPy did not form sheets or micellar-like architectures (Fig. S13 and S18†).

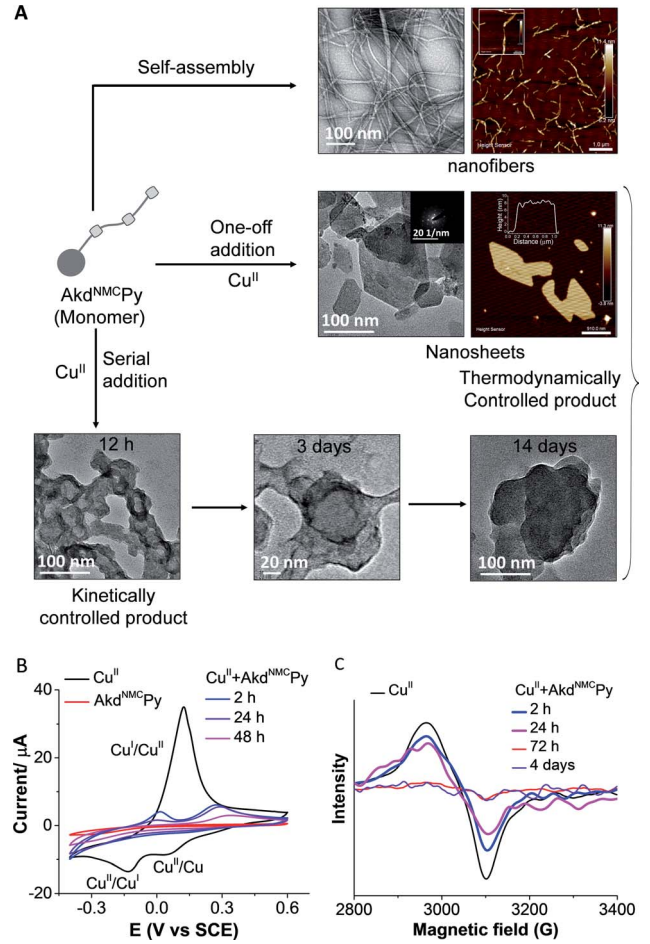

Fig. 3 (A) Differential morphologies of $Akd^{NMC}Py$ in the absence and presence of Cu^{II}. $Akd^{NMC}Py$ self-assembles to form nanofibers. One-off addition of Cu^{II} produced 2D nanosheets (inset: SAED pattern of the sheets), while serial addition formed sheets through intermediate micelle-like core–shell architectures. (B and C) CV and EPR spectra of $Akd^{NMC}Py$ and Cu^{II}, and their complex at various time intervals.

The collective experimental evidence confirmed the binding of $Akd^{NMC}Py$ with Cu^{II} followed by distinct assembly pathways to form nanosheets or micelle-like core–shell architectures which subsequently transformed into thermodynamically stable nanosheets. Next, the binding stoichiometry between $Akd^{NMC}Py$ and Cu^{II}, and the redox behavior of bound Cu ions were studied by liquid chromatography mass spectrometry (LCMS), cyclic voltammetry (CV) and electron paramagnetic resonance (EPR) experiments. Upon addition of Cu^{II}, LCMS spectra showed the gradual disappearance of the $Akd^{NMC}Py$ peak at retention time (t_R) = 7.9 min and the concomitant appearance of a new peak at t_R = 14.8 min (Fig. 2E and Table S2†), which confirmed the equimolar stoichiometric complexation between $Akd^{NMC}Py$ and Cu^{II}. The CV measurements of Cu^{II} solutions after mixing with $Akd^{NMC}Py$ showed a sharp decrease in cathodic (−15 μA at −0.18 V) and anodic (38 μA at 0.13 V) peak current intensities with time. At 48 h incubation with $Akd^{NMC}Py$, the cathodic and anodic peaks of Cu^{II} completely disappeared inferring the complexation-induced decrease of free Cu^{II} in the presence of $Akd^{NMC}Py$ (Fig. 3B). We performed low-temperature EPR spectroscopy measurements to investigate the Cu^{II} coordination environment and oxidation state in the presence of $Akd^{NMC}Py$.[26] The EPR data showed diminishing of the Cu^{II} signal at 3100 gauss (G) in the presence of $Akd^{NMC}Py$ which is attributed to the reduction of Cu^{II} to diamagnetic Cu^{I} (Fig. 3C). Thus, we postulate that complexation of Cu^{II} by $Akd^{NMC}Py$ initially forms micelle-like architectures, which gradually reorganizes to nanosheets guided by the *in situ* reduction of Cu^{II} to Cu^{I}.

Next, we demonstrated the use of distinct architectures of $Akd^{NMC}Py$ as catalytic systems in performing chemical transformations specific to Cu^{II} and Cu^{I}. The catalytic utility of micelle-like architectures of $Akd^{NMC}Py + Cu^{II}$ was investigated in a tandem reaction involving oxidative-hydrolysis of 2′,7′-dichlorofluorescein diacetate (DCFH-DA) (Fig. 4A).[9,27] The micelle-like architectures were prepared by the serial addition of Cu^{II} to $Akd^{NMC}Py$, centrifugation, water washing, and finally dispersed in HEPES buffer (25 mM, pH 8) (Fig. S4†). The oxidative-hydrolysis of DCFH-DA by $Akd^{NMC}Py + Cu^{II}$ was monitored by recording the absorbance of 2′,7′-dichlorofluorescein (DCF) at λ_{max} = 504 nm. The conversion of DCFH-DA into DCF was observed with an initial rate of 8.7 nM min^{-1} (Fig. 4B and S14†). The calculated K_M and catalytic

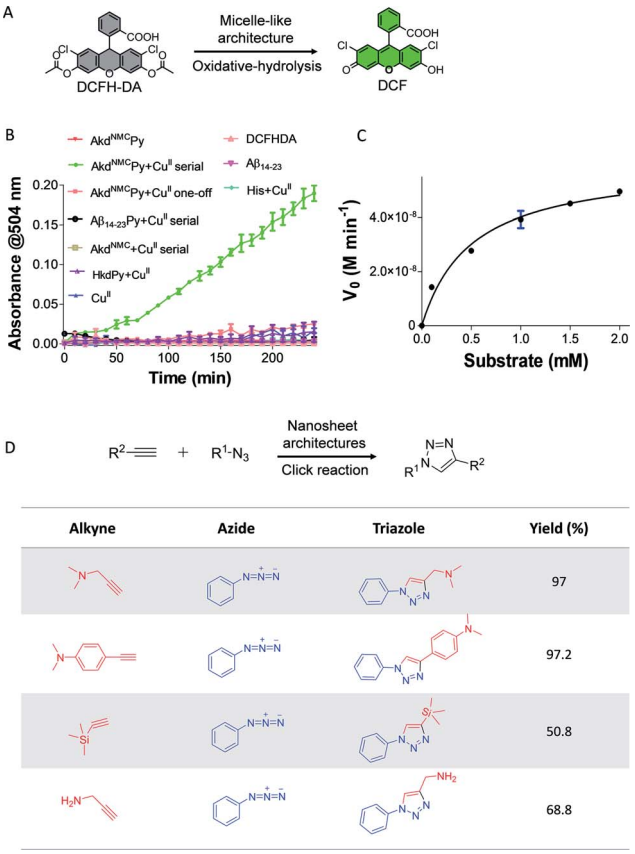

Fig. 4 (A) Micelle-like architectures of catalyzed conversion of DCFH-DA to DCF in HEPES (25 mM, pH 8). (B) Absorbance *vs.* reaction time plots for oxidative-hydrolysis of DCFH-DA catalyzed by micelle-like architectures and other control systems. (C) The plot of initial rate (V_0) *vs.* different substrate (DCFH-DA) concentrations. (D) Alkyne–azide click reaction catalyzed by nanosheets. Substrates with variable substituents and product yields calculated from LC-MS.

efficiency (k_{cat}/K_M) were 0.5 mM and 120 M^{-1} min^{-1}, respectively, which are in agreement with reported peptide-based cascade reactions (Table S3†).[9,27,28] The control reactions revealed that Cu^{II}, His, $Akd^{NMC}Py$, Akd^{NMC}, Aβ14-23, Aβ14-23Py and HkdPy were catalytically inefficient under similar assay conditions (Fig. 4B).

Finally, we evaluated the activity of nanosheets of $Akd^{NMC}Py$ in the Cu^{I}-catalyzed alkyne–azide cycloaddition (CuAAC) reaction to form triazole products.[29] The nanosheets were found to efficiently catalyze the reaction with varied combinations of azide and alkyne to yield 1,4-cycloaddition products as shown in Fig. 4D. The triazole adducts were quantitatively analyzed and characterized by LCMS (Table S4†). The product started forming within 10 min and reached completion by 60 min, as was monitored by NMR spectroscopy (Fig. 4D and S16†). Our study further revealed that nanosheet architectures of $Akd^{NMC}Py + Cu^{I}$ catalyze CuAAC reactions with a considerably faster rate and excellent yields compared to a standard $CuSO_4$ + sodium ascorbate catalyst system (Fig. S15 and S17†). The detailed results from various spectroscopy techniques, oxidative-hydrolysis of DCFH-DA and CuAAC reactions confirmed the stabilization of the Cu^{II} state in micelle-like architectures and *in situ* reductions of Cu^{II} to Cu^{I} in nanosheets of $Akd^{NMC}Py$.

We postulate that the complexation of Cu^{II} with $Akd^{NMC}Py$ initially forms micelle-like architectures, which gradually reorganize into nanosheets guided by the *in situ* reduction of the Cu^{II} to the Cu^{I} state. In one-off addition, the assembly of $Akd^{NMC}Py$ guided by the immediate complexation and reduction of Cu^{II} to Cu^{I} produces thermodynamically stable nanosheet architectures. On the other hand, serial addition led to the controlled complexation of $Akd^{NMC}Py$ to Cu^{II} resulting in step-by-step or cascade assembly processes, which forms meta-stable (kinetically controlled) micelle-like core–shell architectures. These meta-stable architectures finally transformed into thermodynamically stable nanosheets upon complete complexation and reduction of the Cu^{II} to the Cu^{I} state. The observed differential stabilization of copper oxidation states through the generation of distinct architectural forms allowed us to exploit their functional activity towards Cu^{II} and Cu^{I} catalysed oxidative-hydrolytic tandem, and alkyne–azide click reactions, respectively.

Conclusions

In summary, we demonstrated CDP and Cu-directed molecular architectonics of $Akd^{NMC}Py$ to form functional material architectures that differentially modulate Cu-oxidation states and catalytic activities. The fibrillar assembly of $Akd^{NMC}Py$ was engineered into thermodynamically stable nanosheets or kinetically controlled micelle-like architectures by one-off or serial additions of Cu^{II} to $Akd^{NMC}Py$. The experimental studies showed that micelle-like architectures and nanosheets of $Akd^{NMC}Py$ differentially stabilized Cu^{II} and Cu^{I} states, which were efficient catalytic systems in tandem oxidation-hydrolysis and click reactions, respectively. This work is anticipated to inspire the design of artificial biocatalytic architectures capable of performing multiple chemical transformations. Further, the metal-complexation-guided distinct functional architectures that stabilize different oxidation states could help in understanding the complex redox activities of metalloproteins.

Author contributions

D. G. and T. G. designed the project. D. G. synthesized the compounds and undertook the photophysical studies under the supervision of T. G. and D. G. M. K. and T. G. planned the experiments and analyzed the data. T. M. performed docking studies. D. G. and T. G. wrote the manuscript with input from all the authors.

Conflicts of interest

The authors declare no conflict of interest.

Acknowledgements

Authors thank JNCASR, SwarnaJayanti Fellowship grant (DST/SJF/CSA-02/2015-2016), CEFIPRA grant (IFC/A/62T10-3/2020/

963), DST, SERB grant (CRG/2020/004594), and DBT, India, for financial support, and Mohd Monis Ayyub for CV study, Bappaditya Roy for discussion.

Notes and references

1 M. Avinash and T. Govindaraju, *Acc. Chem. Res.*, 2018, **51**, 414–426.
2 H. Moorthy, L. P. Datta and T. Govindaraju, *Chem.–Asian J.*, 2021, **16**, 423–442.
3 K. Ariga, M. Nishikawa, T. Mori, J. Takeya, L. K. Shrestha and J. P. Hill, *Sci. Technol. Adv. Mater.*, 2019, **20**, 51–95.
4 B. Roy and T. Govindaraju, *Bull. Chem. Soc. Jpn.*, 2019, **92**, 1883–1901.
5 A. Levin, T. A. Hakala, L. Schnaider, G. J. Bernardes, E. Gazit and T. P. Knowles, *Nat. Rev. Chem.*, 2020, **4**, 615–634.
6 K. Ariga and L. K. Shrestha, *APL Mater.*, 2019, **7**, 120903–120912.
7 I. W. Hamley, *Angew. Chem., Int. Ed.*, 2007, **46**, 8128–8147.
8 T. P. Knowles and M. J. Buehler, *Nat. Nanotechnol.*, 2011, **6**, 469–479.
9 Z. Lengyel, C. M. Rufo, Y. S. Moroz, O. V. Makhlynets and I. V. Korendovych, *ACS Catal.*, 2018, **8**, 59–62.
10 C. M. Rufo, Y. S. Moroz, O. V. Moroz, J. Stöhr, T. A. Smith, X. Hu, W. F. DeGrado and I. V. Korendovych, *Nat. Chem.*, 2014, **6**, 303–309.
11 B. Roy, S. Pal and T. Govindaraju, *ACS Appl. Mater. Interfaces*, 2020, **12**, 14057–14063.
12 C. Wang, J. Fei, K. Wang and J. Li, *Angew. Chem., Int. Ed.*, 2020, **59**, 18960–18963.
13 M. Díaz-Caballero, S. Navarro, M. Nuez-Martínez, F. Peccati, L. Rodríguez-Santiago, M. Sodupe, M. Teixidor and S. Ventura, *ACS Catal.*, 2020, **11**, 595–607.
14 C. Balachandra, D. Padhi and T. Govindaraju, *ChemMedChem*, 2021, **16**, 1–31.
15 S. Manchineella and T. Govindaraju, *ChemPlusChem*, 2017, **82**, 88–106.
16 Y. Chen, Y. Yang, A. A. Orr, P. Makam, B. Redko, E. Haimov, Y. Wang, L. J. W. Shimon, S. R. Lazar, M. Ju, P. Tamamis, H. Dong, E. Gazit, *et al.*, *Angew. Chem., Int. Ed.*, 2021, **60**, 17164–17169.
17 P. Faller, C. Hureau and C. Berthoumieu, *Inorg. Chem.*, 2013, **52**, 12193–12206.
18 C. Madhu, C. Voshavar, K. Rajasekhar and T. Govindaraju, *Org. Biomol. Chem.*, 2017, **15**, 3170–3174.
19 E. I. Solomon, D. E. Heppner, E. M. Johnston, J. W. Ginsbach, J. Cirera, M. Qayyum, M. T. Kieber Emmons, C. H. Kjaergaard, R. G. Hadt and L. Tian, *Chem. Rev.*, 2014, **114**, 3659–3853.
20 M. Avinash and T. Govindaraju, *Nanoscale*, 2012, **4**, 6102–6117.
21 I. Insua and J. Montenegro, *J. Am. Chem. Soc.*, 2019, **142**, 300–307.
22 O. Trott and A. J. Olson, *J. Comput. Chem.*, 2010, **31**, 455–461.
23 T. Mondal and B. Mandal, *Chem. Commun.*, 2020, **56**, 2348–2351.
24 N. Giri and S. L. James, *Chem. Commun.*, 2011, **47**, 245–247.
25 M. Pandeeswar, H. Khare, S. Ramakumar and T. Govindaraju, *Chem. Commun.*, 2015, **51**, 8315–8318.
26 O. V. Makhlynets, P. M. Gosavi and I. V. Korendovych, *Angew. Chem., Int. Ed.*, 2016, **55**, 9017–9020.
27 M. Filice and J. M. Palomo, *ACS Catal.*, 2014, **4**, 1588–1598.
28 M. P. Friedmann, V. Torbeev, V. Zelenay, A. Sobol, J. Greenwald and R. Riek, *PLoS One*, 2015, **10**, e0143948.
29 Z. Du, D. Yu, X. Du, P. Scott, J. Ren and X. Qu, *Chem. Sci.*, 2019, **10**, 10343–10350.